

Grigory V. Gelikonov, Valentin M. Gelikonov, Sergey U. Ksenofontov, Andrey N. Morosov, Alexey V. Myakov, Yuri P. Potapov, Veronika V. Saposhnikova, Ekaterina A. Sergeeva, Dmitry V. Shabanov, Natalia M. Shakhova, and Elena V. Zagainova

## Contents

27.1	Compact Optical Coherence Microscope .....	1128
27.1.1	Introduction. Overview of the Main Approaches to OCM Design .....	1128
27.1.2	Interferometer for Compact OCM .....	1130
27.1.3	Development of Broadband Light Source and Interferometer Elements ...	1132
27.1.4	Influence of Light Scattering on OCM Spatial Resolution .....	1135
27.1.5	Electro-mechanical System for Dynamic Focus .....	1138
27.1.6	Digital Signal Processing as a Tool to Improve OCM Resolution .....	1140
27.1.7	Experimental OCM prototype .....	1142
27.1.8	Biomedical Applications .....	1142
27.1.9	Conclusion .....	1144
27.2	A New Optical Coherence Microscope Approach Based on Broadband Digital Holography .....	1144
27.2.1	Introduction .....	1145
27.2.2	Fundamentals of the Technique .....	1146
27.2.3	Experiment .....	1151
27.2.4	Conclusion .....	1154
	References .....	1155

G.V. Gelikonov (✉) • V.M. Gelikonov • S.U. Ksenofontov • A.N. Morosov • A.V. Myakov • Y.P. Potapov • V.V. Saposhnikova • E.A. Sergeeva • D.V. Shabanov • N.M. Shakhova  
Institute of Applied Physics of the Russian Academy of Sciences, Nizhny Novgorod, Russian Federation

e-mail: [grig@ufp.appl.sci-nnov.ru](mailto:grig@ufp.appl.sci-nnov.ru), [gelikon@ufp.appl.sci-nnov.ru](mailto:gelikon@ufp.appl.sci-nnov.ru), [xen@appl.sci-nnov.ru](mailto:xen@appl.sci-nnov.ru),  
[morozov@ufp.appl.sci-nnov.ru](mailto:morozov@ufp.appl.sci-nnov.ru), [Myakov@mera.ru](mailto:Myakov@mera.ru), [p\\_up@mail.ru](mailto:p_up@mail.ru), [rkuranov@yahoo.com](mailto:rkuranov@yahoo.com),  
[sea@ufp.appl.sci-nnov.ru](mailto:sea@ufp.appl.sci-nnov.ru), [dvshab@ufp.appl.sci-nnov.ru](mailto:dvshab@ufp.appl.sci-nnov.ru), [shakh@ufp.appl.sci-nnov.ru](mailto:shakh@ufp.appl.sci-nnov.ru)

E.V. Zagainova

Medical Academy, Nizhny Novgorod, Russian Federation

e-mail: [ezagaynova@gmail.com](mailto:ezagaynova@gmail.com)

---

**Abstract**

This chapter presents the practical embodiment of two types of optical coherence microscope (OCM) modality that differ by probing method. The development and creation of a compact OCM device for imaging internal structures of biological tissue at the cellular level is presented. Ultrahigh axial resolution of 3.4  $\mu\text{m}$  and lateral resolution of 3.9  $\mu\text{m}$  within tissue was attained by combining broadband radiations of two spectrally shifted SLDs and implementing the dynamic focus concept, which allows in-depth scanning of a coherence gate and beam waist synchronously. This OCM prototype is portable and easy to operate; creation of a remote optical probe was feasible due to use of polarization maintaining fiber. The chapter also discusses the results of a theoretical investigation of OCM axial and lateral resolution degradation caused by light scattering in biological tissue. We demonstrate the first OCM images of biological objects using examples of plant and human tissue *ex vivo*.

Another variant of OCM is based on a broadband digital holographic technique. The final section of the chapter concerns 2D or 3D optical coherence tomography (OCT) imaging of the internal structure of strongly scattering media with micrometer-scale resolution by processing 200 sets of 2D holographic complex reconstructions at interference reception of backscattered light obtained at different wavelengths separated by a fixed spectral interval in the wavelength region of tens of nanometers. This technique of internal structure visualization apparently has a number of advantages over the known time-domain and spectral OCT methods, including the absence of transverse scanning systems at 3D visualization, and transverse spatial resolution has no limitations inherent in the correlation and spectral OCT techniques.

---

## 27.1 Compact Optical Coherence Microscope

### 27.1.1 Introduction. Overview of the Main Approaches to OCM Design

Optical coherence microscopy (OCM) is a new biomedical modality for cross-sectional subsurface imaging of biological tissue combining the sectioning abilities of optical coherence tomography (OCT) with confocal microscopy (CM). In OCM, spatial sectioning due to tight focusing of the probing beam and pinhole rejection provided by CM is enhanced by additional longitudinal sectioning provided by OCT coherence gating. For the first time, the OCT technique was used to enhance optical resolution of confocal microscopy by Izatt et al. [1]. Later, the OCM method and its potential for clinical application were studied and discussed in Ref. [2]. In that study, OCM images of a 5- $\mu\text{m}$  layer located at the depth of 500  $\mu\text{m}$  of the normal human colon specimen were acquired. The OCM images clearly demonstrated structures with resolution at the cellular level.

One of the main challenges of OCM is to provide high axial resolution by means of ultra-broadband light sources. As in OCT, the longitudinal resolution in OCM depends on bandwidth of a light source. Axial OCM resolution at a subcellular level was reported in Ref. [3], where a Kerr-lens mode-locked Ti:sapphire laser with double-chirped mirrors with a bandwidth up to 350 nm was used. At the wavelength of 0.8  $\mu\text{m}$ , the authors attained 1- $\mu\text{m}$  longitudinal resolution and 3- $\mu\text{m}$  transverse resolution in biotissue. In Ref. [4], a superluminescent Ti:Al<sub>2</sub>O<sub>3</sub> crystal was demonstrated as a possible light source for ultra-high-resolution OCT. This new source yielded light with power of 40  $\mu\text{W}$  and bandwidth of 138 nm, which provided longitudinal resolution of 2.2  $\mu\text{m}$  in air and 1.7  $\mu\text{m}$  in tissue.

The feasibility of ultra-high axial resolution using supercontinuum generation was demonstrated by Hartl et al. [5]. The authors developed a broadband OCT imaging system with bandwidth of 370 nm and central wavelength of 1.3  $\mu\text{m}$ . The longitudinal resolution of 2.5  $\mu\text{m}$  in air and 2  $\mu\text{m}$  in tissue was attained. An unprecedented axial resolution using supercontinuum generation was reported in Ref. [6]. The optical spectrum of generated light extended from 550 to 950 nm ( $\lambda = 725$  nm,  $P_{out} = 27$  mW); the corresponding axial resolution in air was 0.75 and 0.5  $\mu\text{m}$  in biological tissue.

Nowadays, semiconductor diodes are the most compact broadband IR light sources. In Ref. [7], the authors combined radiations of several broadband luminescent diodes (LEDs) in order to improve longitudinal resolution of OCM by broadening the probing light spectrum. As a result, resolution was sufficient to successfully image microspheres with a diameter of 6  $\mu\text{m}$  up to the depth of 500  $\mu\text{m}$  in a scattering medium containing a suspension of 0.2- $\mu\text{m}$  particles. For the same purpose of improving axial resolution, radiations of two superluminescent diodes (SLDs) with central wavelengths separated by 25 nm (830 and 855 nm, respectively) were combined [8]. The effective bandwidth of 50 nm was achieved, which corresponded to axial resolution of 6–7  $\mu\text{m}$  in tissue. Although the semiconductor sources cannot yet provide axial resolution attainable by other sources, the field of IR optics is nevertheless rapidly evolving.

A second major challenge in OCM is to perform synchronous axial scanning of a sharply focused focal spot and the coherence gate while keeping their spatial alignment constant. For this purpose, in Refs. [1] and [2], the object itself was moved through a high-aperture lens and OCM images of a thin layer of the object near the focal area were acquired. In Refs. [3] and [4], several individual images obtained with the focus at different depths were fused to yield a composite image. The problem of synchronous scanning was partially solved when the dynamic focus method was proposed [6, 7]. In this method, the coherence gate and the sharply focused area of the probing beam are spatially aligned and moved in the axial direction simultaneously. In some designs the dynamic focus was attained by mounting an output objective of the signal arm and a retroreflector in the reference arm on the same scanning platform. However, this schematic provides satisfactory results only for relatively short scanning distances, because the mismatch between the coherence gate and sharply focused area is compensated only partially. In the alternative approach of dynamic coherence focus described in Ref. [9], the optical

length of the sample arm does not change during scanning. As a result, the coherence gate remains in the beam focus, requiring no additional adjustment of the reference arm. In Ref. [10], the authors describe another realization of the method for precise alignment of the focal area and coherence gate. Synchronous scanning is attained by moving the tip of the output fiber and a lens inside of the objective. This approach was successfully applied to determine refractive indices of different subsurface layers of biological tissue *in vivo*.

In our study we developed and fabricated a prototype of a compact OCM with a flexible sample arm and a remote optical probe for laboratory and clinical environment. To achieve axial resolution at the cellular level, a light source with effective bandwidth of 100 nm was developed. It comprised two semiconductor SLDs based on one-layer quantum-dimensional (GaAl)As-heterostructures with shifted spectra. Radiations from both SLDs were coupled into polarization-maintaining (PM) fiber by means of a specially designed multiplexer. The multiplexer was spectrally adjusted in order to achieve the minimum width of auto-correlation function (ACF). To broaden the bandwidth of a Michelson interferometer, the polished coupler based on anisotropic fiber with broadband of 3 dB was developed.

We also solved the problem of the dynamic focus by scanning the output lens of the objective located at the very end of the sample arm. The lens movement was controlled by the electronic system, thus allowing alignment of the sharply focused focal spot with the coherence gate spatially during their simultaneous scanning depth of 0.5–0.8 mm in biological tissue.

A method for suppression of spectral side lobes caused by non-uniformity of the light source spectrum was developed and successfully applied; the suppression efficiency was also estimated.

In addition, the problem of light propagation in a scattering medium was solved numerically. The dependence of axial resolution on the probing depth was studied for different parameters of the scattering and absorbing medium and the incident spectrum of probing radiation.

### 27.1.2 Interferometer for Compact OCM

A diagram of a compact OCM interferometer based on the traditional OCT scheme using PM fiber is shown in Fig. 27.1. The fiber optical Michelson interferometer employed for OCM comprises sample and reference arms. The use of anisotropic fiber allows the signal arm to be flexible, which is important for clinical applications. A light source consisted of two SLDs based on one-layer quantum-dimensional (GaAl)As-heterostructures with central wavelengths of 907 and 948 nm, bandwidths of approximately 53.4 and 72 nm, and initial power of 0.9 and 3 mW, respectively.

The probing light produced by the light source is passed through the sample arm to the optical probe. The probe comprises the optical and mechanical systems that perform focusing of the beam and also axial and lateral scanning. At the same time, the probe collects light backscattered by the object. The reference arm delivers

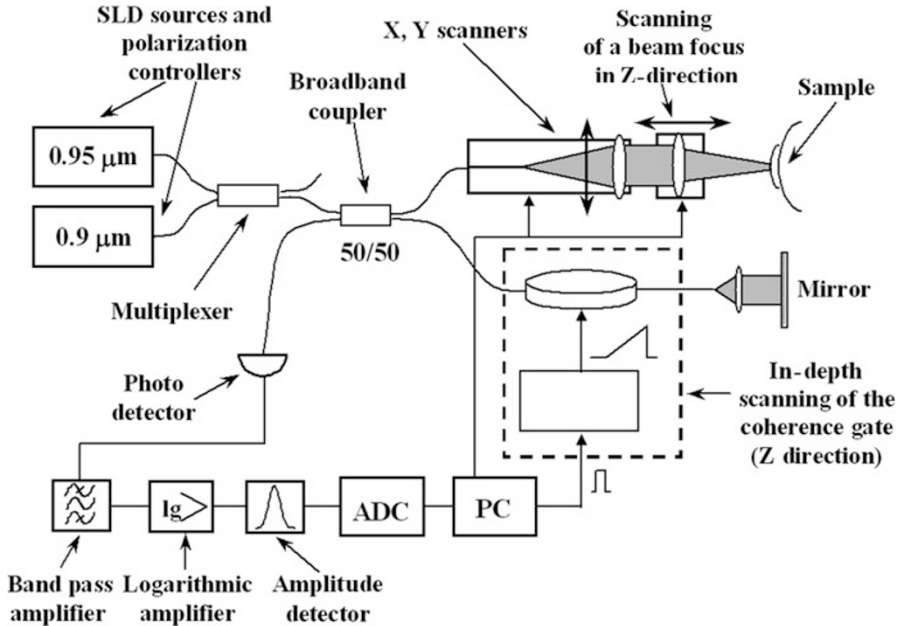


**Fig. 27.1** OCM functional scheme

light onto a reference mirror and transports it back to the beamsplitter. At the beamsplitter, the light from both arms of the interferometer is combined. The light backscattered by the object would produce interference fringes with light reflected from the reference mirror only if the path-length difference between the arms does not exceed the coherence length of the source. The interference fringes are detected by the photo diode. The path-length difference between the arms of the interferometer ( $\Delta L$ ) was modulated by a linear law  $\Delta L = \Delta \dot{L} \cdot t$  to perform heterodyne detection of the interference signal. This was attained by elastically stretching and contracting in antiphase the fibers using modulators based on piezoelectric converters [11]. In this case, the probing depth  $h$  inside of the object, from which the signal is measured, varies at a rate  $\dot{h} = \Delta \dot{L} \frac{n_{fgr}}{n_{mgr}}$ , where  $n_{fgr}$  and  $n_{mgr}$  are group-refractive indices of a fiber material and the object, respectively. When the path-length difference between the arms is changed linearly at the rate of  $\Delta \dot{L}$ , optical frequencies in the interferometer arms differ by a value of the Doppler shift. Therefore, the interference signal contains the component at a Doppler frequency  $F = \frac{2\Delta \dot{L} n_f}{\lambda_0} = 2n_{mgr} \frac{\dot{h}}{\lambda_0} \frac{n_f}{n_{fgr}}$ , where  $n_f$  is the fiber phase refractive index, and  $\lambda_0$  is the vacuum wavelength of probing radiation. For instance, at the wavelength of  $0.94 \mu\text{m}$  and the Doppler frequency of  $0.4 \text{ MHz}$  the optical path-length difference between the interferometer arms is changed at the rate of  $\Delta \dot{L} n_f \sim 0.13 \text{ m/s}$ .

The optical probe comprises a scanner that provides the “dynamic focus” by longitudinally scanning an output lens of the objective in the axial direction. The

scanner also moves the probing beam in the lateral directions, thus, generating both 2D and 3D images. The optical layout of a scanner consists of a two-lens objective; therefore allowing use of the maximum numerical aperture of the output lens. The objective magnification is equal to unity; the diameter of the focal spot is less than 4  $\mu\text{m}$ . In the current design, the effective “dynamic focus” is implemented up to the depths at which sharp beam focusing starts to degrade due to multiple scattering of light.

Movement of an optical beam along the object surface is attained by moving an additional lens of the objective transversely. Scanning is performed by an electro-mechanical system that is incorporated into an optical probe at the end of the sample arm of the interferometer. The scanning process is fully automated and computer controlled.

The interference signal was detected using a photo diode with a fiber optical input characterized by a high quantum yield ( $>0.8$ ) and low noise level. After analog processing, the signal is fed to a computer through an analog-digital converter. The computer is further utilized for digital signal processing, recording, and displaying of images.

According to the scheme of signal detection and analog processing, the resulting signal comprises a component that is proportional to the logarithm of the coefficient of tissue backscattering. The two-dimensional field of tissue backscattering coefficient obtained by scanning in depth (by changing the optical path-length difference between the interferometer arms) and along the object surface (by moving the probing beam laterally) is displayed on a computer monitor and stored for further processing. In contrast to many other indirect modalities of imaging of turbid media, reconstruction of both OCT and OCM images from the measured signal does not require solution of the complex inverse problem. Each in-depth element of an image corresponds to the certain time of light propagation to this element and back, i.e., the certain path-length difference between the interferometer arms. Therefore, the obtained images are relatively easy to interpret because they do not require any post processing and can be displayed in real time during scanning.

### **27.1.3 Development of Broadband Light Source and Interferometer Elements**

Miniature superluminescent emitters and fiber elements of the interferometer are the basis for creation of compact portable devices that are suitable for clinical and industrial environments. The superluminescent semiconductor diodes based on one-layer quantum-dimensional (GaAl)As-heterostructures with central wavelengths of 907 and 948 nm, spectral widths of about 53.4 and 72 nm, and initial radiation power in the output of the single-mode fibers of 0.9 and 3 mW were employed as a light source. Spectra and corresponding ACFs of SLDs used are shown in [Fig. 27.2](#).

The spectra of the both SLDs have complicated shapes that are inherent for quantum-dimensional heterostructures [[12](#), [13](#)]. When the radiations of two SLDs are mixed, the spectrum of resulting radiation considerably depends on the ratio of initial powers of each SLD. [Figure 27.3a](#) illustrates several resulting spectra

**Fig. 27.2** (a) Spectral characteristics of superluminescent diodes. (b) Autocorrelation functions

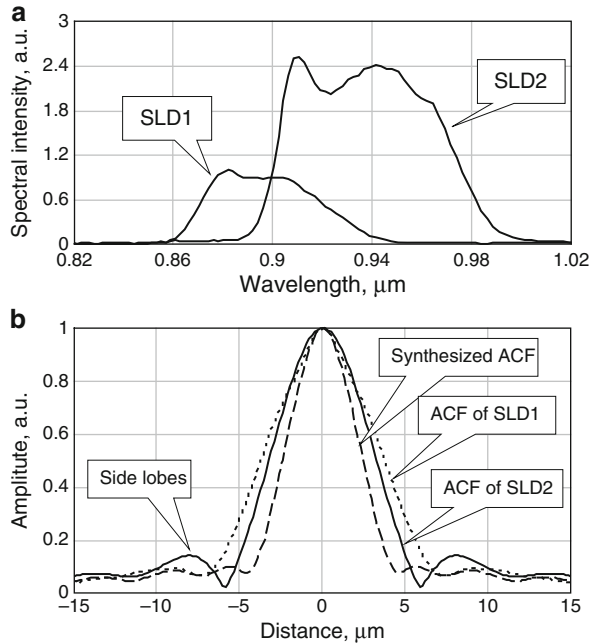


**Fig. 27.3** Synthesis of broadband signal at different values of attenuation factor  $\alpha$  of the second source (SLD2). (a) Synthesized spectrum, (b) corresponding autocorrelation function

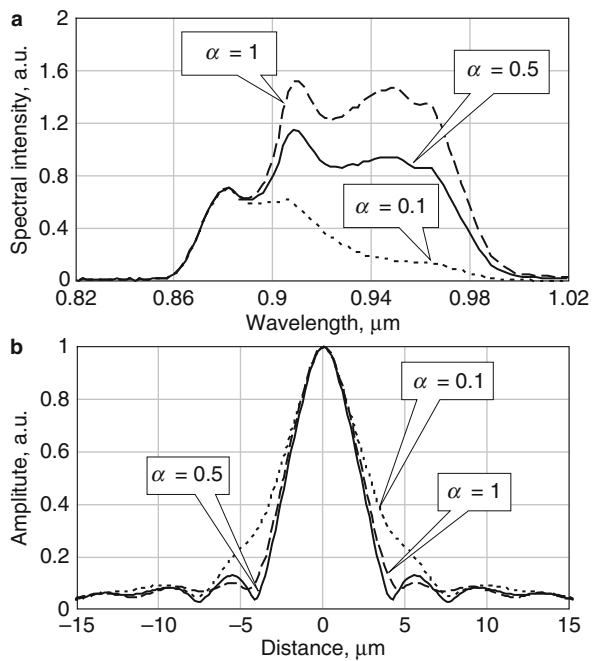
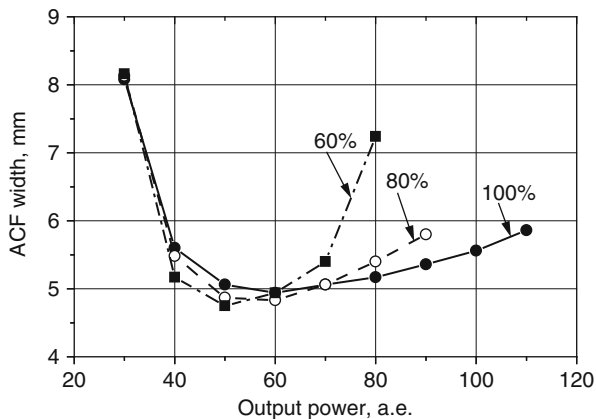


**Fig. 27.4** Dependence of resulting ACF width versus output power of the multiplexer



obtained at the fixed power (0.9 mW) of a 907 nm SLD and varying power of a 948 nm SLD (relative attenuation  $\alpha$  of the initial power of the 948 nm SLD is attained by lowering the pumping current). Corresponding ACFs are shown in Fig. 27.3b. The resulting optimal spectrum was of a complex shape; bandwidth of generated light was slightly wider than 100 nm and corresponding minimum width of the central ACF lobe was 4.9  $\mu\text{m}$  (free space). The side lobes of ACF were suppressed to the level of 17.5 dB as compared to the central main peak.

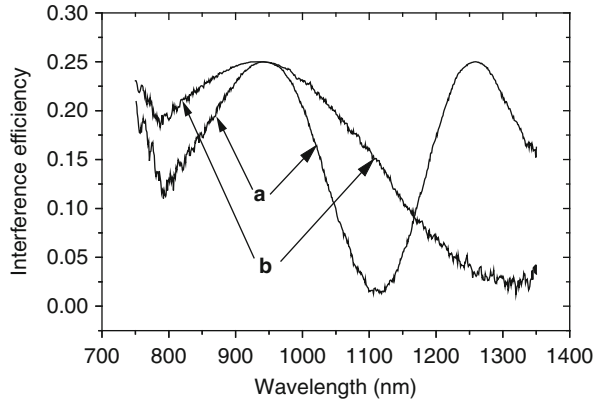
Spectral tuning of the fiber optic multiplexer combining optical radiations from two SLDs in one fiber was found to be critical. By controlling the parameters of the multiplexer during assembly, the multiplexer output was optimized to provide the narrowest ACF, which automatically provided the widest bandwidth of the resulting spectrum. The multiplexer was made of halves of a polished coupler using anisotropic fiber. The final assembly of the multiplexer was performed with light introduced into both halves; the output ACF of the resulting radiation was controlled with a correlometer and optimized as described above until the minimum width of the resulting ACF was attained.

Figure 27.4 shows several curves of the resulting ACF width versus total output power of the multiplexer. Parameter  $\alpha$  was a ratio of current power of 948 nm SLD to the initial power of 3 mW. The narrowest achieved ACF width corresponded to 4.75  $\mu\text{m}$  in air.

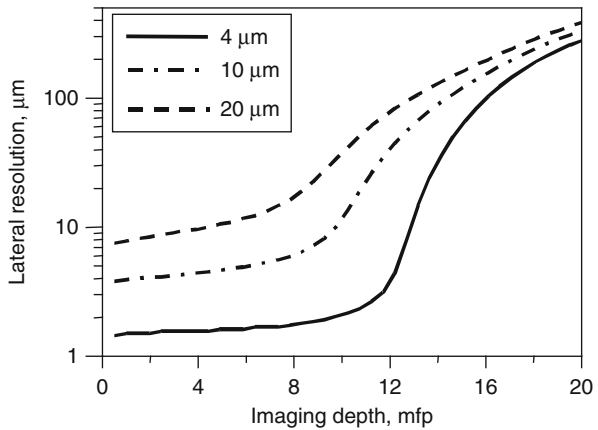
The interferometer comprised a fiber optical 3-dB coupler built of polished elements. There was observed optical coupling of modes in the polished elements due to interaction of exponentially decreasing fields occurring mostly in fiber coating. Polished couplers in contrast to welded ones usually provide a higher degree of isolation of polarization modes with the extinction coefficient of at least 35 dB. However, typical couplers of this type have bandwidths that are insufficiently wide for use in interferometers with bandwidths of light sources at the order of 100 nm. In our study, we analyzed the possibility of increasing the broadband of the 3-dB coupler by optimizing its parameters. As a result, we determined a more optimal domain of parameters and developed a 3-dB coupler



**Fig. 27.5** Coupling efficiency, forward and backward pass, (a) with conventional broadbandness, and (b) enhanced broadbandness



**Fig. 27.6** Dependence of OCM lateral resolution versus depth for different initial waist sizes of probing beam

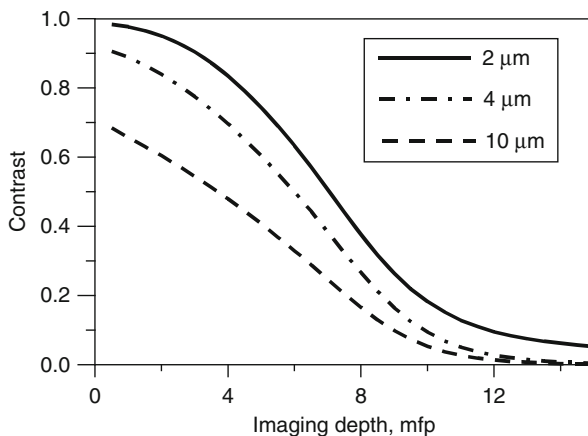


with improved broadband. Figure 27.5 presents experimental curves of the transfer coefficient during successive propagation and coupling in conventional and novel couplers. As can be seen from the graph, the novel design provides broadband approximately twice that of a conventional design. The parameters of the novel 3-dB fiber optical coupler are listed below: spectral bandwidth of 150 nm with central wavelength of 0.94 μm, insertion losses less than 0.2 dB, and the level of cross-talk between the polarization modes less than 35 dB.

### 27.1.4 Influence of Light Scattering on OCM Spatial Resolution

Multiple small-angle scattering affects spatial resolution of the OCM method significantly. In the transparent non-scattering medium, in-depth spatial resolution of the method is defined by a longitudinal coherence length ( $l_c$ ) that is related to a coherence time ( $\tau_c$ ) and the velocity of light in the medium ( $v_n$ ):  $l_c = \frac{v_n \tau_c}{2}$ . OCM sub-micron lateral resolution is determined by the waist size of the probing beam

**Fig. 27.7** The contrast of the layer with spatially modulated backscattering coefficient for various initial beam waist sizes



and is attained by using large numerical apertures. However, at typical imaging depths within biological tissue, multiple small-angle scattering becomes the dominant reason responsible for reducing the quality of obtained OCM images. Owing to multiple small-angle scattering, the radius of the focal spot increases, thus resulting in degradation of OCM lateral resolution. Moreover, the phenomenon of small-angle scattering also decreases OCM axial resolution due to multipass of photons.

However, the analysis of OCM resolution performed on the basis of the above-discussed theoretical model allows us to conclude that loss of spatial resolution due to scattering can be reduced by strong focusing of the probing beam, and in this way both lateral and axial resolution can be improved.

Figure 27.6 shows a dependence of OCM lateral resolution versus imaging depth for various waist sizes of the probing beam waist. It is assumed that an OCM image is reconstructed by synchronous in-depth scanning of the beam focal spot and the length of the reference arm while keeping the beam waist size constant. The lateral resolution was estimated by the FWHM of an OCM image of a point object obtained from the theoretical OCT model described in ► Chap. 24 (► Sect. 24.2) [14, 15]. (All presented dependences are calculated for a medium with scattering coefficient  $\mu_s = 10 \text{ mm}^{-1}$ , anisotropy factor  $g = 0.9$ , and initial longitudinal coherence length  $l_c = 5 \text{ }\mu\text{m}$ .) As is seen from the Fig. 27.6, OCM lateral resolution is preserved for larger imaging depths for probing beams with smaller initial sizes of beam waists. Starting from 10 mean free paths (mfp), a considerable loss of lateral resolution occurs due to diffuse widening of the probing beam at the focal depth. Under these conditions, the focusing effect also disappears and the behavior of lateral resolution versus depth becomes asymptotic and universal for all initial sizes of beam waists.

The idea of how OCM lateral resolution is lost can be deduced from imaging the layer with sinusoidal spatial modulation of the backscattering coefficient. Figure 27.7 demonstrates contrast of such a structure, i.e., the relative modulation amplitude of detected intensity versus the layer depth within scattering medium.

**Fig. 27.8** OCM axial resolution versus the imaging depth for different waist sizes of probing beam

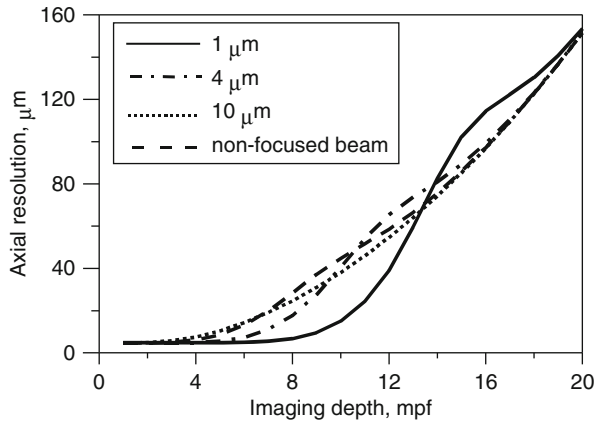
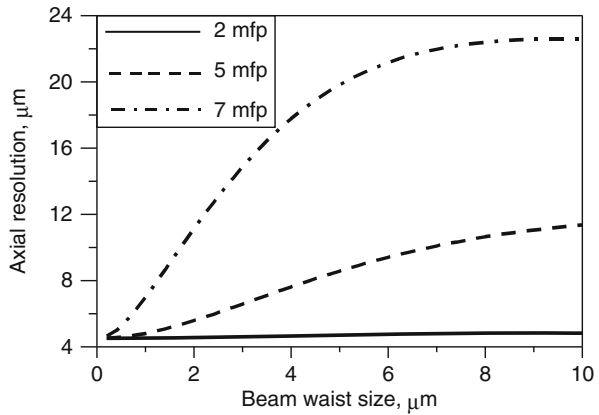


**Fig. 27.9** OCM resolution degradation versus beam waist size at various imaging depths



The contrast depends on the structure scale significantly. At shallow depth, the structures for which the scale is comparable to the size of the beam waist have far less contrast than those with the scale on the order of 10 diameters of the beam waist. Contrast degradation with the imaging depth can be explained by beam widening at the focal volume, the beam waist first becomes comparable with the structure scale and then exceeds it.

It is important to point out that axial resolution of the method of OCM benefits from tight focusing of the probing beam due to retaining of the longitudinal coherence length for larger imaging depth in comparison to non-focused or weakly focused beams. OCM axial resolution is defined as the width of an OCM image of a thin backscattering layer. Figure 27.8 shows the dependence of OCM axial resolution on the imaging depth for different sizes of beam waists. At shallow depth, strong focusing provides better axial resolution because ballistic photons of a highly focused beam contribute greater to the total light distribution at the focal

volume. However, at larger depths one can notice a sharper decrease of axial resolution for beams with smaller widths. This effect can originate from the fact that, for a beam focused deep inside of a scattering medium, the backscattered OCM signal is registered not from the focal volume precisely but from a closer distance due to group retardation of photons. In the case of tight focusing, the beam volume that contributes to the detected signal is larger than that of a weakly focused beam. Therefore, the OCM image is formed by photons undergoing more scattering events, which results in a significant loss of axial resolution. Figure 27.9 shows the behavior of OCM axial resolution for various imaging depths as the beam waist increases.

In summary, the analysis of OCM spatial resolution shows that tight focusing of the probing beam allows preserving both lateral and axial resolution up to the depth of 10 mfp due to increased contribution of ballistic photons to an OCM signal.

### 27.1.5 Electro-mechanical System for Dynamic Focus

The optical probe comprising the focusing system and the means for transversal beam scanning is located at the distal end of the sample arm of the interferometer. The optical layout of the focusing system consists of two lenses with effective magnification of unity. The lateral focal spot size was equal to 3.9  $\mu\text{m}$ , i.e., to the diameter of fiber mode of the sample arm. The second lens allows using the objective aperture with maximum efficiency. The dynamic focus is attained in this OCM prototype by moving the output lens axially and thus providing longitudinal movement of the focal spot through the object (Fig. 27.10a). The relationship between the axial displacement of the focal spot in a medium and the coherence gate while they are simultaneously scanned and the path-length difference between the arms of the interferometer is established below. If the focal spot during lens scanning is placed inside of a uniform medium with a refractive index  $n$ , then, as shown in Ref. [9], the lens displacement  $\Delta z_L$  will correspond to the increase in the optical path length of the sample arm by  $nn_g\Delta z_L$ . Here,  $n_g$  is the group refractive index of the medium. Therefore, when the lens is moved, the distance between centers of the focal and coherence zones gets shifted by  $nn_g\Delta z_L$ . In our interferometer, an additional modulator is used to scan the optical path-length difference between the interferometer arms [11]. The path length difference of  $\Delta z$  in free space corresponds to the displacement of the coherence zone in the medium of  $\Delta z/n_g$ . Obviously, the initially aligned focal spot and coherence gate centers will not diverge during scanning only if the following condition is satisfied  $nn_g\Delta z_L = \Delta z$ . At the fixed rate of the path length difference scanning that determines a Doppler frequency, the rate of the axial movement of the output lens should be  $\Delta \dot{z}_L = \Delta \dot{z}/(n \cdot n_g)$ .

The typical length of the focal area (Rayleigh waist), say, for a focal spot diameter of 3.9  $\mu\text{m}$  is 26  $\mu\text{m}$ . Therefore, spatial alignment of the coherence gate and the focal spot should be quite accurate. The output lens was hanged in flexible suspension and scanned according to the triangular law by an electromagnetic

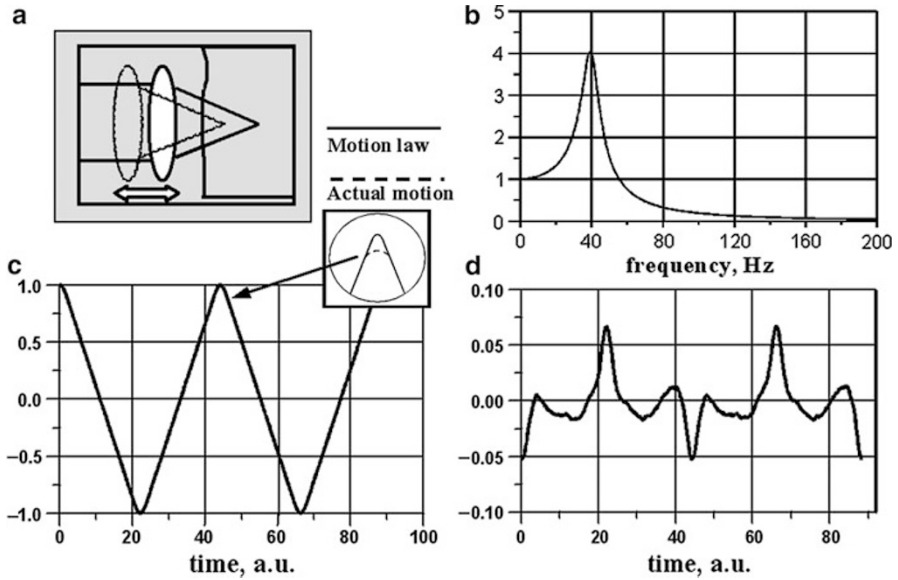


**Fig. 27.10** Dynamic focusing in OCM

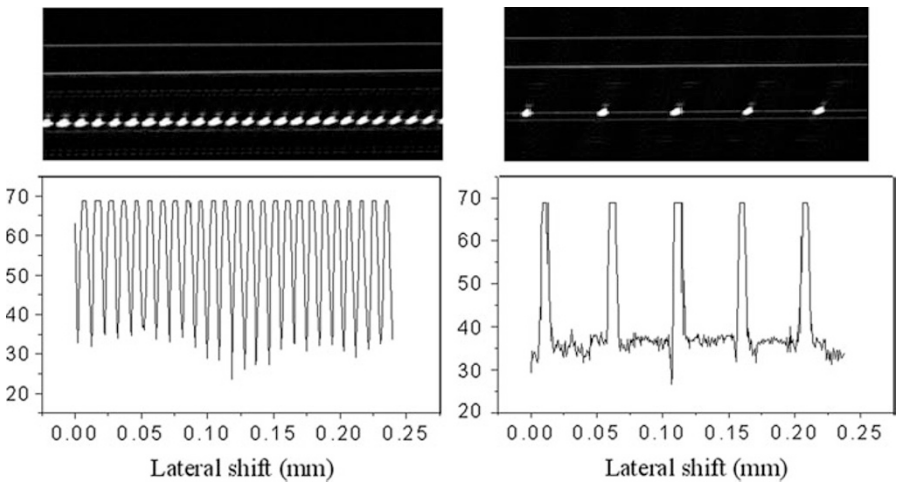


**Fig. 27.11** OCM images of periodic patterns

controller with frequency of 100 Hz (Fig. 27.10c). The amplitude-frequency characteristic of the mechanical system was typical for resonance mechanical systems with a resonance frequency of  $\sim 40$  Hz and a Q factor of  $\sim 4$  (Fig. 27.10b). Since the frequency of lens scanning was close to the resonance frequency of the system, the control triangular signal was pre-distorted to compensate for the resonance response. As a result, it was measured that for the amplitude of

lens oscillations of 0.6 mm, the difference between the real motion and the theoretical one did not exceed 2 % for approximately 80 % of the movement range (Fig. 27.10d). The lateral resolution of OCM was analyzed using a grating with a step of 10  $\mu\text{m}$ . The OCM images of the periodic pattern were recorded for several longitudinal positions of the sample. In a typical image shown in Fig. 27.11, the contrast of the image is about 30 dB. This corresponds well with the computational results for a Gaussian beam with a waist of 3.9  $\mu\text{m}$  in diameter.

Of course, it is not always possible to precisely align the coherence gate and focal zone in real biotissue. This can be caused by deviations of refraction index from its mean, which are typical for biotissue layers [10]. In fairly thick layers of biological tissue, the misalignment can exceed the size of the focal zone. However, this misalignment can be eliminated in a single layer by correcting the lens movement law. To obtain an image with maximum resolution over the whole scanning range, it is necessary to acquire several 2D images with corrected focusing for particular layers of biological tissue and then fuse these 2D images.

### 27.1.6 Digital Signal Processing as a Tool to Improve OCM Resolution

As was described in Sect. 27.1.2, the radiation from two spectrally separated SLDs was combined in one fiber. It was observed that the resulting radiation had a spectrum of a non-Gaussian shape. This phenomenon led to the appearance of side lobes in ACF at the distance of  $\pm 10 \mu\text{m}$  from the main center peak with amplitude of  $-18 \text{ dB}$ . To suppress the side lobes, we developed a method of regularization of the spectrum of the Doppler signal by means of digital signal processing. The idea of the method is to devise a regularization function that could be used to multiply the original ACF with side lobes and the product would yield ACF with nearly Gaussian shape with suppressed side lobes. Using this function, the recorded radio-frequency (RF) signal was converted and an OCM image was reconstructed.

Figure 27.12 shows the ACF shape before and after spectrum regularization. It can be seen that the side lobes were suppressed approximately by 17 dB. Figure 27.13 presents spectra of the Doppler signal before and after regularization and the spectrum of the regularizing function. Note that along with the correction of the spectrum, the regularization procedure eliminated noise outside of the Doppler detection band. Figure 27.14 illustrates an example of an OCM signal from two thin scattering boundaries separated from each other by 18  $\mu\text{m}$ , before and after regularization.

It can be seen from this figure that the side lobes of responses from two boundaries overlap. Obviously, the resulting side lobes in the OCM signal in between the central peaks of boundary responses depend on the phase difference between the latter. As a result, the suppression of these combined side lobes by means of regularization would also depend on a distance between responses. In this

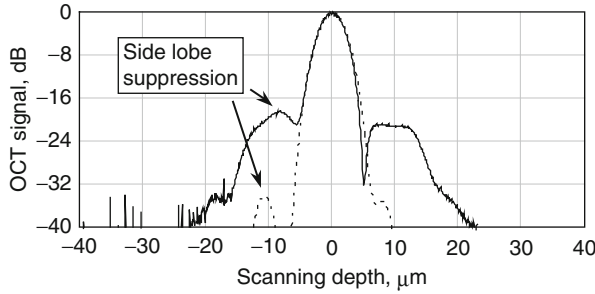


**Fig. 27.12** Autocorrelation function before (*bold line*) and after (*dotted line*) regularization procedure

**Fig. 27.13** Spectra of the Doppler signal before (*bold solid line*) and after regularization (*bold dotted line*) and the spectrum of the regularizing function (*solid thin line*)

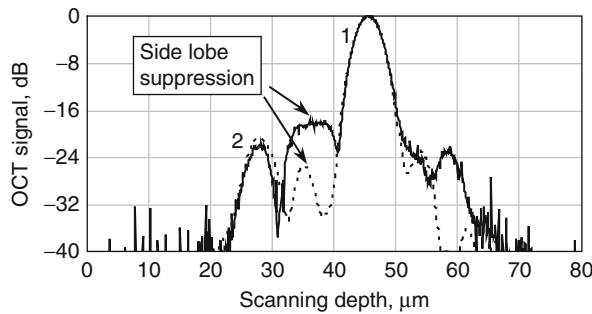
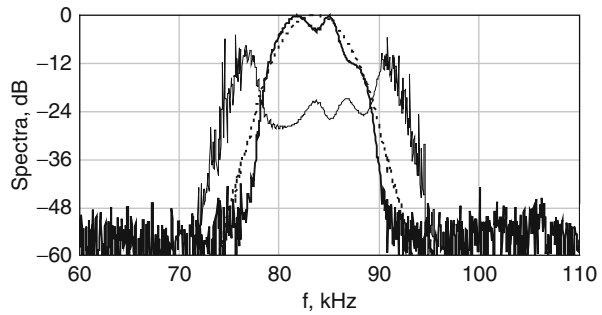


**Fig. 27.14** *Bold line*: OCT signal obtained from two reflectors, peaks 1 and 2, correspondingly; *dotted line*: OCT signal after spectra regularization procedure. The amplitude of a side lobe between peaks 1 and 2 is larger than the amplitude of peaks 2 and thus produces a false target on a tomogram. Regularization method allows one to suppress side lobes significantly

particular case, the side lobes were suppressed by 8 dB. If the distance between neighboring imaging elements exceeds the coherence length, the degree of side lobe suppression by regularization will be the same as for ACF and will be equal to 17 dB.

**Fig. 27.15** General view of OCM



### 27.1.7 Experimental OCM prototype

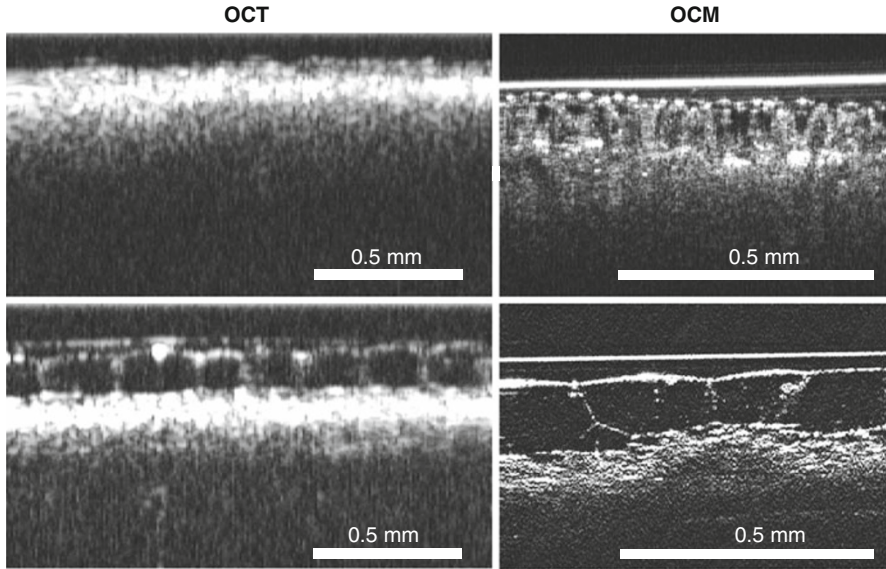
All the ideas and approaches described above were implemented in our experimental compact OCM prototype. The OCM setup features a flexible signal arm and a remote optical probe at the distal end. The probe is equipped with a three-coordinate scanning device that controls a focal zone position. The size of the optical probe in the largest dimension does not exceed 5 cm. The studied object is placed atop the output window with immersion. Figure 27.15 presents a general view of the compact optical coherence microscope and the remote optical probe connected to the main body by flexible optical and electrical cables. The dimensions of the OCM device in this configuration do not exceed  $12 \times 30 \times 40 \text{ cm}^2$ , weight is about 7 kg. The OCM requires standard AC power network, device power consumption is no more than 25 W. The OCM device can be operated and images can be recorded and stored using a personal desktop or portable computer with a processor 486DX-33 or higher. The OCM device in the current design may be applied for intraoperative express analysis of human tissues *ex vivo*.

### 27.1.8 Biomedical Applications

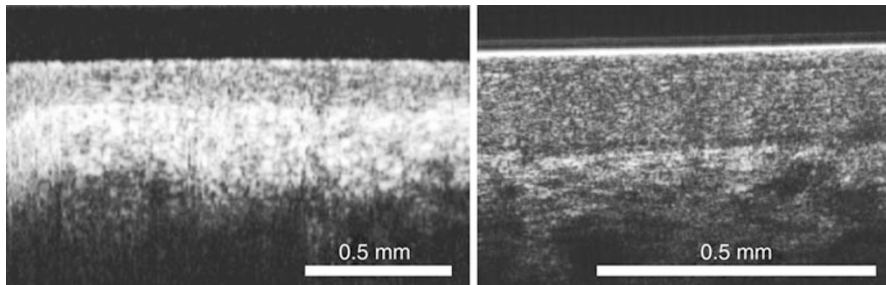
Preliminary biomedical experiments using OCM were carried out on model media and on biological materials *ex vivo*, namely, plant leaves and excised human tissues were studied. Plant leaves were observed immediately after separation from the stem in order to minimize influence of a decrease in cellular turgor on the quality of images. Postoperative samples of human tissue were placed into physiological solution right after excision and were studied during next 40 min. to avoid postmortal tissue alterations.

Figure 27.16 shows OCM and OCT images of tomato and tradescantia leaves. Images clearly demonstrate morphological features of studied objects. Advantages of OCM over OCT are obvious: while OCT allows differentiation of mostly cellular





**Fig. 27.16** OCT and OCM images of tomato and tradescantia leaves



**Fig. 27.17** OCT and OCM images of uterine cervix ex vivo

layers, and rarely large cells with a size of 50–100  $\mu\text{m}$ , OCM easily visualize both cellular layers and single cells with a size of 10–20  $\mu\text{m}$  constituting these layers.

Quality of visualization of intracellular structures is determined not only by spatial resolution of the method but also by the chosen plane of scanning because sometime 2D scans miss cellular nuclei. 3D scanning of the object with a step of several microns between the 2D planes allowed reconstruction of the true 3D structure of the object, detecting cellular nuclei and accurate estimating of cellular shapes and sizes.

Based on our experience with OCT where the most informative were tissues with a stratified internal structure for the OCM study we chose organs covered with the squamous epithelium. The idea of the study was to compare OCM and OCT performances. Results of the study are shown in Fig. 27.17. Comparative analysis

revealed that while standard OCT could visualize the tissue layers, namely, the epithelium and underlying stroma, OCM could distinguish single cells constituting the epithelium up to depth of 500  $\mu\text{m}$ .

Therefore, clinical and biological experiments clearly demonstrate that spatial resolution of OCM is sufficient for visualizing single cells. High spatial resolution of OCM advances us to the realization of the idea of absolutely non-invasive “optical” biopsy. We believe that another promising application of OCM is monitoring of plants *in vivo* with a purpose of dynamic control of structural alterations. Non-invasive investigation of internal structures of plants would allow studying the influence of various environmental factors (external and internal). Such studies would definitely benefit selections, ecology, and cosmic biology.

### **27.1.9 Conclusion**

This part of the chapter presents development and fabrication of a compact OCM based on broadband PM fiber elements. OCM combines advantages of ultra-broadband OCT and high numerical aperture confocal microscopy. An ultra-broadband light source was devised and constructed using two SLDs with spectra covering the wavelength range of 0.88–0.98  $\mu\text{m}$ . The light source provided axial resolution of 4.75  $\mu\text{m}$  in air. The optical layout of the OCM probe comprised two micro lenses transposing the fiber tip with magnification of 0.8–1 and provided lateral resolution of about 3.9  $\mu\text{m}$ . The focal volume of the probing beam and the coherence gate were spatially matched and scanned in-depth synchronously using the principle of the dynamic focus. For this purpose we developed and created a three-coordinate electro-mechanical system. We also proposed and investigated a method for correction of distortion of the ACF form caused by the non-Gaussian shape of the light source spectrum. This method corrects the envelope shape and suppresses the spectral side lobes by regularizing the spectrum of the Doppler signal at the stage of digital signal processing. The dependences of axial and lateral spatial resolutions of the optical coherence microscope on imaging depth in media with scattering parameters typical for tissue were investigated theoretically. OCM images of model media and biological objects *ex vivo* were acquired.

---

## **27.2 A New Optical Coherence Microscope Approach Based on Broadband Digital Holography**

The broadband digital holographic method allows getting high-resolution 3D images of depth structure of biotissue (or other turbid matters) by IR radiation without axial and lateral scanning. Absence of any mechanical scanning, unlike time domain (TD) and spectral domain (SD) OCT methods, removes restriction on time of reception of 3D OCT images.

### 27.2.1 Introduction

Much attention has been given to developing methods for visualizing internal structure of biological objects such as optically turbid layered media with spatial resolution of several microns. These include time domain (correlation) OCT [16] and spectral OCT [17] based on low-coherence interferometry, as well as confocal microscopy (CM) [18]. Cross-sectional, micron-scale imaging of internal structure of the studied object is based on reception of a spatially localized component of backscattered and back-reflected radiation with suppression of the influence of background noisy multiple scattering. A raster (2D) pattern of cross-sectional imaging is attained by means of transverse scanning. The use of transverse scanning with lens translation in low-coherence interferometry gave rise to both, the term OCT and the OCT technique [16]. Later, transverse scanning was accomplished by including various systems driving a fiber tip, e.g., [19], as well as some other mechanical methods [20]. Scanning methods as well as principles of formation of longitudinal and transverse elements of spatial resolution are different in different OCT modalities and CM, hence, limitations and drawbacks of the latter are also different, which can be illustrated by some examples. For instance, in the time domain OCT technique, a probing wave beam is formed with Rayleigh length equal to the entire observation length so as to ensure uniform illumination of the object. Scattered light at each time instant can be received only from the region whose depth is equal to the radiation coherence length [16] and is much smaller than the Rayleigh length. As the scattered radiation components coming from other regions do not take part in interference, the power of probing optical radiation is used inefficiently. In the spectral OCT technique, each received spectral component has equivalent coherence length exceeding a possible area of study, and optical power is used more effectively. The drawback of this technique is a possibility of coherent noise [21, 22]. Confocal microscopy [18] has higher longitudinal and transverse resolution but the signal decays faster with increasing observation depth than in the case of OCT. Note that for CM and OCT depth enhancement, the method of optical clearing is currently under way [23–25]. The OCM technique that combines the principles of OCT and CM [1, 26] provides larger observation depth and better spatial resolution. A second major challenge in OCM is to perform synchronous axial scanning of a sharply focused focal spot and the coherence gate while keeping their spatial alignment constant. The difficulties encountered with the use of the OCM technique relate mainly to accuracy of controlling the focusing lens motion, especially when scanning multilayered biological objects. The transverse and longitudinal scanning systems in all of the above-mentioned techniques are based on mechanical devices whose resonance properties limit the speed and accuracy of motion. In addition, some applications, such as endoscopy, demand compact systems for transverse scanning that may introduce additional difficulties.

Some papers address development of a method for visualizing 3D objects without longitudinal and transverse scanning. Holographic reception of scattered

light is used for digital 2D or 3D imaging of the object [27–29]. For example, the method of determining complex amplitude of the field scattered from an object holographically recorded on CCD matrix is described in the Ref. [27], where the image of a flat object recorded in monochromatic light at the wavelength of 514 nm was reconstructed. The longitudinal position of the object was set to an accuracy of Rayleigh length of effective Gaussian beam determined by the size of the CCD matrix and distance to the object. Longitudinal spatial resolution in the holographic method may be increased by processing a series of holograms obtained at different wavelengths separated by a fixed spectral interval [28, 29]. Thus, the spatial resolution of 3 cm obtained in [28] using 11 holograms in the 10 GHz laser-tuned interval (595 nm central wavelength) allowed resolving two plane layers spaced 18 cm apart. A method of transverse spatial harmonics expansion for 3D imaging from a hologram was described in [29]. It was demonstrated that this method has better processing speed and signal-to-noise ratio than imaging by the Fresnel diffraction formula for different distances between the object and the hologram. For example, surface structure of a coin was reconstructed from 20 holograms obtained in the 575–605 nm wavelength range. Thus, fundamental principles of using holographic photoreceiver matrix records of scattered light for digital 2D and 3D imaging of object surfaces were considered in [27–29].

The holographic method of recording interference pattern and subsequent digital reconstruction and imaging of the object may be employed in the OCT technique for imaging the internal structure of scattering media (biological objects). In conventional holography an object is illuminated by a monochromatic source of light, and the result of interference between the light scattered or refracted by the object surfaces and the reference wave is 2D recorded. Holographic imaging of several semitransparent internal structures is also possible. Rayleigh length is an element of longitudinal spatial resolution in 3D imaging. One of the ways to further improve longitudinal spatial resolution is to use low-coherence radiation similarly to the time domain [16] and spectral [17] OCT techniques. Still another resource for increasing longitudinal spatial resolution in holographic recording is reduction of effective Rayleigh length by increasing the angular aperture of scattered light reception like in confocal microscopy [18], which is especially interesting for detailed drafting of small-size objects [30].

The goal of the current work is implementation in experiments with a broadband digital OCT holographic technique for visualizing external and internal structure of layered scattering media with a resolution of several microns and analysis of its merits and drawbacks.

## 27.2.2 Fundamentals of the Technique

In the current work, as in [27–29], information about backscattered radiation was obtained by means of 2D recording of a holographic picture instead of transverse X-Y scanning by probing light. Longitudinal resolution was enhanced, similarly to [28, 29], using a series of holograms recorded at several wavelengths

separated by a fixed spectral interval in a broad spectral band. Probing and reference waves had spherical and plane wave fronts, respectively.

In a digital hologram, a signal of each matrix element is proportional to optical field intensity. Two-dimensional records of the signal represented for simplicity in continuous coordinates may be written in the following form:

$$S(x, y) = I_R(x, y) + I_S(x, y) + 2 \cdot \sqrt{I_R(x, y) \cdot I_S(x, y)} \cdot \cos[\varphi_R(x, y) - \varphi_S(x, y)], \quad (27.1)$$

where  $I_R(x, y)$ ,  $I_S(x, y)$  are the intensities at the  $(x, y)$  point on the CCD-matrix plane of the reference and scattered wave fields, respectively, and  $\varphi_R(x, y)$  and  $\varphi_S(x, y)$  are the phases of these fields. In addition, for simplicity, we omitted in the interference term in formula (27.1) the visibility factor numerically equal to the cosine of the angle between wave vectors of the interfering waves. The quantities entering (27.1) are real; however, complex representation of the signal is needed to remove conjugate components for image reconstruction. For this it is necessary to make three digital sets of records of signals from the CCD matrix with the phase difference between the waves  $\Delta\varphi = 0, \pi/2$  and  $\pi$ . By subtracting the result of the first records from the second one, and of the second from the third, and taking into account that the reference wave intensity and phase are independent of the transverse coordinate, we obtain the following two expressions:

$$\begin{aligned} S_2(x, y) - S_1(x, y) &= \sqrt{2} \cdot A_S(x, y) \cdot \cos(\varphi_S(x, y) - C) \text{ and} \\ S_3(x, y) - S_2(x, y) &= \sqrt{2} \cdot A_S(x, y) \cdot \sin(\varphi_S(x, y) - C), \end{aligned} \quad (27.2a)$$

where  $C = \text{const} + \frac{3\pi}{4}$ , and  $A_S(x, y) = \sqrt{I_S(x, y)}$  is the amplitude of the field.

Expressions (27.2a) may be transformed to a complex form of the field in the CCD-matrix plane  $S_C(x, y)$ :

$$S_C(x, y) = A_S(x, y) \cdot \exp(i \cdot \varphi_S(x, y) - C). \quad (27.2b)$$

The field at the object site at distance  $z$  from the CCD-matrix plane is reconstructed as follows. First, the field scattered by the object must be expanded in terms of plane waves at  $z = 0$ . For this the  $S_C(x, y)$  field is 2D Fourier transformed:

$$FFF2d_C(k_x, k_y)_0 = \iint S_C(x, y) \cdot \exp(i \cdot k_x \cdot x + i \cdot k_y \cdot y) \cdot dx \cdot dy, \quad (27.3)$$

where  $k_x, k_y$  are the transverse spatial frequencies that are projections of the wave vectors of these plane waves on the X and Y axes, respectively. With such a digital hologram representation, the conditions of Kotelnikov-Nyquist's criterion should

be met for transverse spatial harmonics of the field scattered by an object. The absolute value of wave vector projections onto the XY-plane of the matrix should not exceed  $\frac{\pi}{d}$ , where  $d$  is the size of the matrix element. This condition determines the magnitude of minimal distance to the object.

As the observation plane is moving from the matrix plane along the Z-axis, the complex value of the 2D Fourier transform (27.3) for a definite direction in the  $k$ -representation ( $k_x, k_y, k_z$ ) will only change the phase with velocity  $\partial\phi/\partial z = k_z$ . The resulting 2D Fourier transform in the  $z$ -plane has the form

$$FFF2d_c(k_x, k_y)_z = FFF2d_c(k_x, k_y)_0 \cdot \exp(-i \cdot z \cdot \sqrt{k^2 - k_x^2 - k_y^2}). \quad (27.4)$$

The inverse Fourier transform of the  $FFF2d_c(k_x, k_y)_z$  array gives the representation of the field from the object at distance  $z$  from the CCD matrix at the wavelength  $\lambda = 2 \cdot \pi/k$ .

Figure 27.18 shows the real part of the reconstructed field for different depths  $z$ , presented in intensity scale for a single scattering object.

The resolution attained with such a technique may be calculated (approximately) by formulas for the transverse  $2\omega_0$  and longitudinal size  $2Z_R$  of the waist of the Gaussian beam focused by a lens having diameter  $d$  equal to the size of the CCD matrix and focal distance  $f$  equal to the distance from the matrix to the object, respectively:

$$2 \cdot \omega_0 = \frac{4 \cdot \lambda}{\pi} \cdot \left(\frac{f}{d}\right), \quad (27.5)$$

$$2 \cdot Z_R = \frac{\pi \cdot 4 \cdot \omega_0^2}{2 \cdot \lambda}. \quad (27.6)$$

Note that the radiation coherence length of a tunable source should exceed the depth of the studied area. To increase longitudinal in-depth resolution (along  $z$ ), like in spectral OCT, the radiation source with spectral bandwidth  $\delta\lambda$  should be tuned discretely within the spectral range  $\Delta\lambda$  with step  $\Delta\lambda/N$ . As a result, using the procedure described above one can obtain  $N$  complex holograms for this set of  $N$  wavelengths. The result of 3D field distribution in complex form is calculated for each  $n$ -th wavelength. 3D representation of the signal  $S_C(x, y, z)$  is calculated by summarizing in complex form all  $N$  3D field distributions obtained above:

$$S_C(x, y, z) = \sum_{n=1}^N \iint FFF2d_C(k_x, k_y, \frac{2\pi}{\lambda_n}) \cdot \exp(-i \cdot z \cdot \sqrt{\left(\frac{2\pi}{\lambda_n}\right)^2 - k_x^2 - k_y^2}) \cdot \exp(-i \cdot k_x \cdot x - i \cdot k_y \cdot y) \cdot dk_x \cdot dk_y, \quad (27.7)$$

which allows increasing resolution along the  $z$ -axis at 3D imaging. In our case, when  $k^2 \gg k_x^2 + k_y^2$ , expression (27.7) may be simplified as follows:

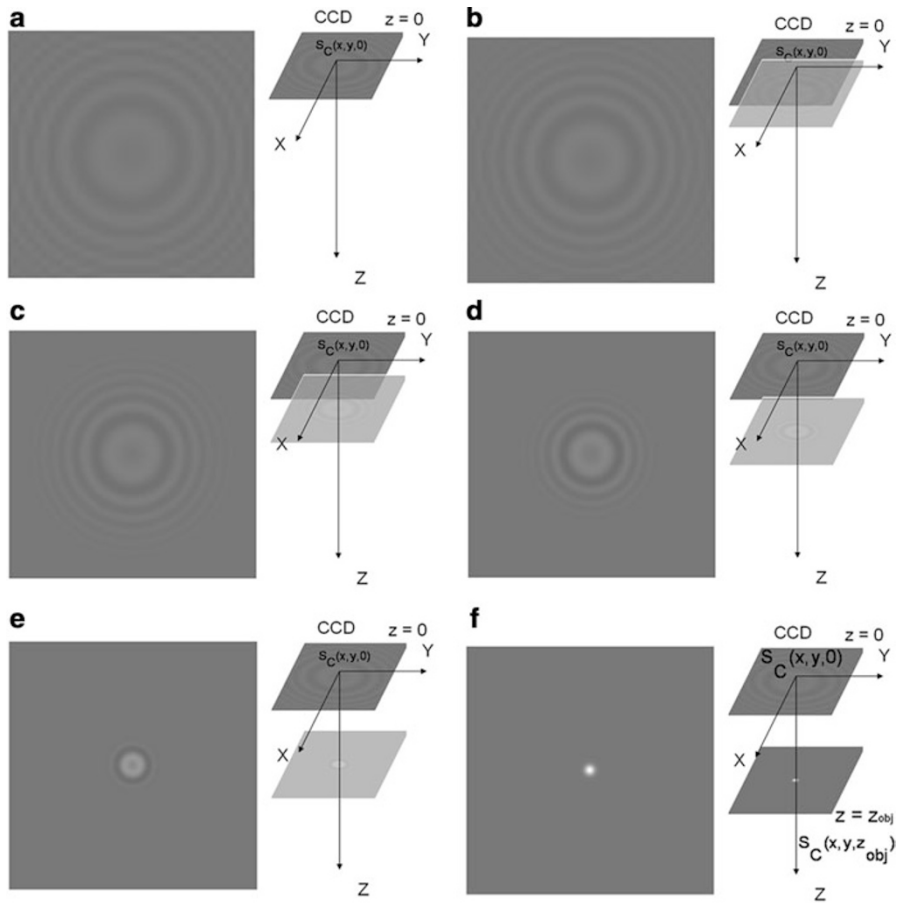


**Fig. 27.18** 2D optical field reconstruction for different  $z$  – distance to CCD plane. Fragment f corresponds to scatterer location

$z \cdot \sqrt{k^2 - k_x^2 - k_y^2} \approx k \cdot z - z_0 \cdot \frac{k_x^2 + k_y^2}{2 \cdot k^2}$ , where  $z_0$  is the coordinate of the object border.

Thus, expression (27.7) is represented as a 3D Fourier transform written for simplicity in integral form

$$S_C(x, y, z) = \iiint FFF3d_C(k_x, k_y, k) \cdot \exp(-i \cdot k_x \cdot x - i \cdot k_y \cdot y - i \cdot k \cdot z) \cdot dk_x \cdot dk_y \cdot dk. \tag{27.8}$$

Formula (27.8) is calculated by a standard algorithm of fast Fourier transform. Here



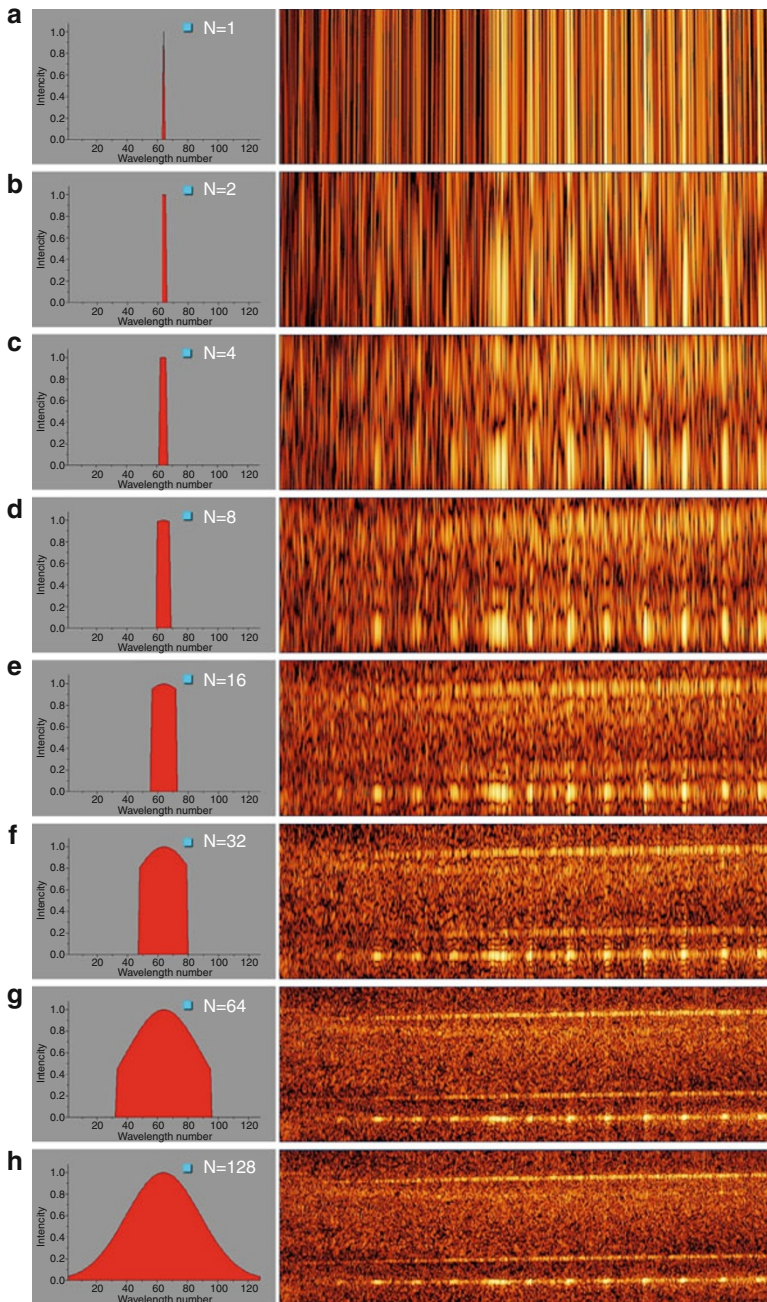
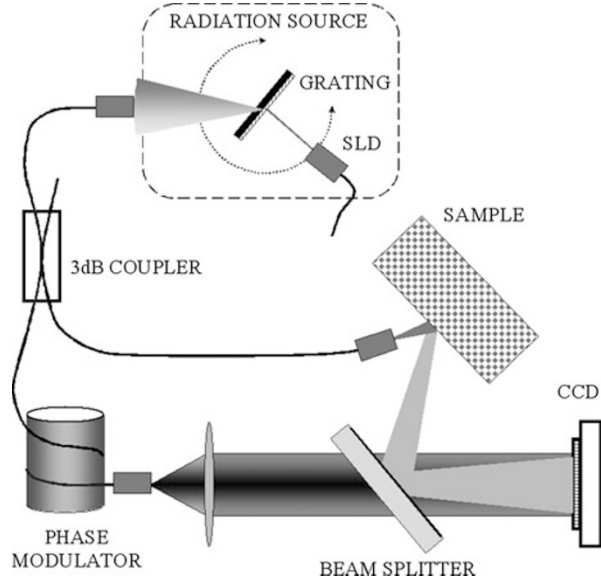


**Fig. 27.19** Dependence of axial resolution on the number of spectral lines registered independently. Left column – spectral shapes; right column – X-Z planes of the corresponding reconstructions of “metric circle crosshair contact reticle”



**Fig. 27.20** Optical scheme of the holographic OCT technique



$$FFT3d_C(k_x, k_y, k) = FFT2d_C(k_x, k_y, k) \cdot \exp\left(i \cdot z_0 \cdot \frac{k_x^2 + k_y^2}{2 \cdot k}\right)$$

Note that, unlike the holographic image obtained by means of monochromatic radiation, a multiwave 3D image has longitudinal spatial distribution determined by the width of the spectral range of light source tuning

$$\Delta z = \frac{2 \cdot \ln 2}{\pi} \cdot \left(\frac{\lambda^2}{\Delta \lambda}\right),$$

rather than by equivalent Rayleigh length.

Experimentally, Fig. 27.19 demonstrates the decreasing of axial resolution element while increasing of a number  $N$  of spectral lines registered independently.

### 27.2.3 Experiment

The setup for implementing the holographic OCT technique is shown schematically in Fig. 27.20.

A prototype of a narrowband radiation source with coherence wavelength of several millimeters (2–3 mm) tuned in the 30-nm spectral range with the central wavelength of 850 nm was created for the experiment. Radiation of a broadband superluminescent source was subjected to spectral discrimination with a diffraction grating (1,200 grooves per millimeter) and, further, radiation in the spectral interval

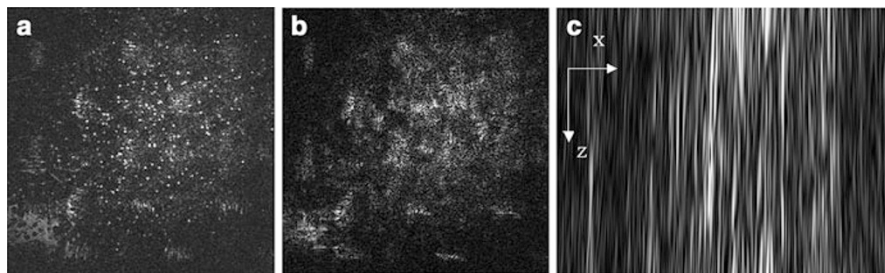


**Fig. 27.21** Image of the object section in the planes  $z = 43$  mm (a),  $z = 44$  mm (b), and result of in-depth section imaging (in the  $x$ - $z$  plane) in the 42–44 mm interval (c)

$\delta\lambda$  was collimated into a single-mode fiber. The operating wavelength was changed by the collimator angle of turn relative to the grating. The source radiation power was about  $2 \mu\text{W}$ .

Wavelength tunable IR radiation was separated by means of a fiber optic coupler (Fig. 27.20) into a probing and a reference wave in 9/1 ratio. The probing wave was emitted into free space from a single-mode fiber with natural divergence determined by the mode size. The reference wave that was also emitted into free space was then collimated into a plane wave. The wave scattered by the object was added to the reference wave on the CCD matrix that recorded the result of their interference. In our experiment we used a CCD matrix with  $1024 \times 768$  elements, each being  $4.65 \times 4.65 \mu\text{m}$  in size. With such a density of matrix elements, the Kotelnikov-Nyquist's criterion was met at distances to the object not less than 40 mm. An example of digital reconstruction of field amplitude from complex holograms recorded at one wavelength is shown in Fig. 27.21 for a fiberglass plastic sample – scattering material with coarse-fiber structure located 43 mm away from the CCD matrix. Pictures of the reconstructed field  $2.37 \times 2.37$  mm in size ( $500 \times 500$  points) for the surface of the object ( $z = 43$  mm) in the transverse  $x$ - $y$  plane are shown in Fig. 27.21a, and for the section 1-mm deep inside the object ( $z = 44$  mm) in Fig. 27.21b.

The first section corresponding to the surface of the object shows the image of surface micro-inhomogeneities with diffraction resolution. This is due to location of the object's surface near the focus of the equivalent confocal system digitally reconstructed from one complex hologram. The image in the second section corresponds to detuning from the focal plane by the depth of about  $10 \cdot Z_R$ .

The in-depth reconstruction of the cross-section (in the  $x$ - $z$  plane) for the same studied sample is presented in Fig. 27.21c, where  $z$  (the vertical axis) varies from 42 to 44 mm, the size along the horizontal is 2.37 mm. This plane image is reconstructed from a complex hologram using a coherence source at  $0.85 \mu\text{m}$ . The extended structures represent the Rayleigh regions (27.6)  $2 \cdot Z_R$  in size. Here, the longitudinal resolution is analogous to confocal reception. In our case, for  $\lambda = 0.85 \mu\text{m}$ ,  $f = 43$  mm, and  $d = 5$  mm we have:  $2 \cdot \omega_0 \approx 10 \mu\text{m}$  and  $2 \cdot Z_R \approx 200 \mu\text{m}$ . It is clear from Fig. 27.21 that the holographic image obtained at one length has good transverse and poor longitudinal resolution.

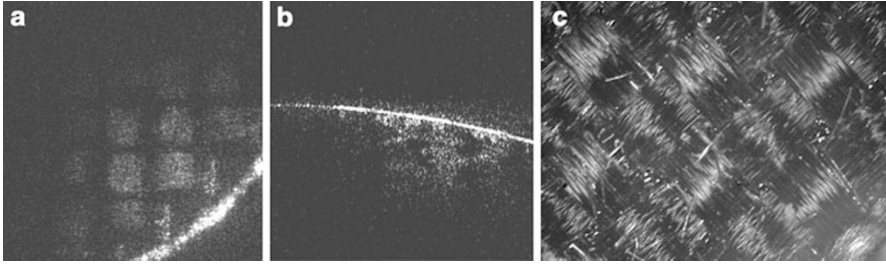


**Fig. 27.22** Reconstructed fragments of bulk image in the X-Y plane (a) and in the X-Z plane (b). (c) Photographic image of the object, cleft in plane X-Y on the same depth

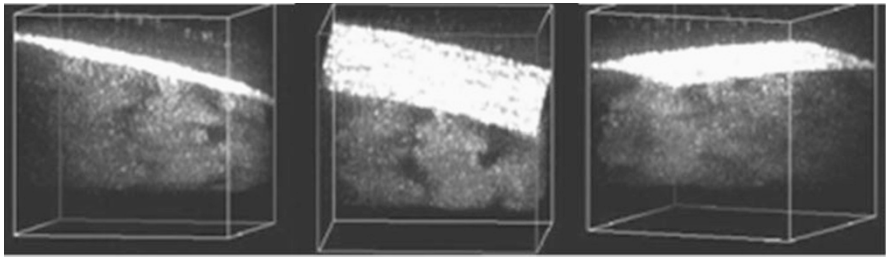


**Fig. 27.23** Fragments fiberglass plastic 3D images under different angles of observation

To increase resolution along the  $z$ -coordinate we obtained 200 complex holograms using the procedure described above for equidistant wavelengths in the 30 nm spectral range with center at  $0.85 \mu\text{m}$ . The fragments of bulk image reconstructed by formula (27.7) are given in Fig. 27.22 in the form of two sections (parallel and normal to its surface) at the depth of  $\sim 0.5 \text{ mm}$ .

The regions of the object in Fig. 27.22 have the size of  $2.5 \times 2.5 \text{ mm}$ . Figure 27.22 demonstrates potentialities of digital image reconstruction with high spatial resolution from a series of complex holograms obtained without a focusing system. In our case, for the effective value  $\Delta\lambda = 30 \text{ nm}$ , the theoretical maximum of longitudinal spatial resolution is  $\Delta z \approx 11 \mu\text{m}$ .

In Fig. 27.23, various projections of fiberglass plastic 3D image obtained in a Mach-Zehnder interferometer setup are presented. Images are presented for various angles of observation for the object part, bounded in  $x$ - $y$  plane (approximately  $1 \times 1 \text{ mm}$ ). On images through the artificial cube lateral sides, the fiberglass plastic internal structure is visible.

The surface curvature visible in the figures is attributed to probing wave divergence and may be removed by means of the corresponding correction during imaging.

Other images were obtained using commercial tunable laser source BS840-02 by Superlum (Russia). Output optical power is about 1 mW, tuning range is from 825 to 875 nm, and laser line width is  $\delta\lambda = 0.1 \text{ nm}$ . The test object was comprised of

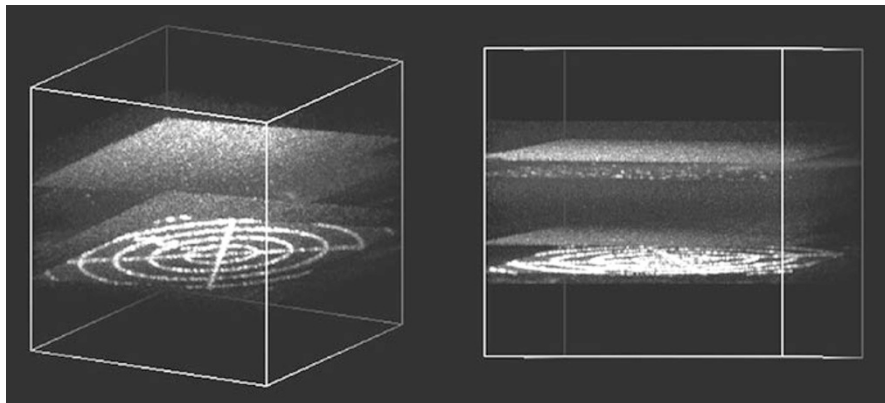


**Fig. 27.24** 3D images of the test object acquired with a tunable laser source

a NT39-454 Metric circle crosshair contact reticle (Edmund Optics) and piece of semitransparent tape on the surface. Some fragments of the 3D image of the test object are represented in [Fig. 27.24](#).

#### 27.2.4 Conclusion

In this chapter we presented results of development of two versions of the OCM technique based on low-coherence interferometry. First, we described results of creating OCM in which time-domain OCT and confocal microscopy are combined. One of the principal features of this OCM variety is the use of several scanning systems for high spatial resolution imaging (3-4  $\mu\text{m}$ ) along the X,Y,Z coordinates. These include the transverse scanning system and the system of synchronous axial scanning of a sharply focused focal spot and a coherence gate while keeping their spatial alignment constant.

In the second part of the chapter we considered practical application of OCM technique based on broadband digital holography. Thus, this chapter described further development of the earlier research [27–29, 31]. Full-range 3D OCT imaging of in-depth layered structure of the object is based on the digital holographic method of recording scattered signal using a wavelength-tunable IR radiation source and digital reconstruction.

This technique of internal structure visualization apparently has a number of advantages over the known TD-OCT [16] and SD-OCT [17] methods. Firstly, digital holographic recording of scattered signal in OCT eliminates the need in transverse scanning systems for 3D visualization, as well as systems of longitudinal scanning of a sharply focused focal spot and a coherence gate. Secondly, holographic recording ensures a much larger reception aperture of scattered radiation and higher signal-to-noise ratio. In the third place, transverse spatial resolution has no limitations inherent in the correlation and spectral OCT techniques. Resolution

can be improved up to the wavelength (and even submicron) size when using a large digital-aperture lens or small pixel size of the matrix. The considered broadband digital holographic technique is a good instrument for investigation of biological objects. But it is important to ensure fast hologram recording to eliminate the influence of phase disturbance by living objects moving during the total exposure time. With the state-of-the-art computer speed, a 3D image with 512 elements along each coordinate may be processed during about 1 sec.

**Acknowledgments** The authors thank Alexander Turkin and Pavel Morozov for assistance in creating optical elements, Irina Andronova for valuable scientific discussion, Nadezhda Krivatkina and Lidia Kozina for providing translation, and Marina Chernobrovtszeva for editing. This work was partly supported by the Russian Foundation for Basic Research under the grants #01-02-17721, #03-02-17253, #03-02-06420 and by the Civilian Research & Development Foundation under the grant RB2-2389-NN-02 and State Contract No. 02.740.11.0516 of March 15, 2010.

---

## References

1. J.A. Izatt, M.R. Hee, G.M. Owen, E.A. Swanson, J.G. Fujimoto, Optical coherence microscopy in scattering media. *Opt. Lett.* **19**, 590–592 (1994)
2. J.A. Izatt, M.D. Kulkarni, H.-W. Wang, K. Kobayashi, M.V. Sivak Jr., Optical coherence tomography and microscopy in gastrointestinal tissues. *IEEE J. Sel. Top. Quant. Electron.* **2**, 1017–1028 (1996)
3. W. Drexler, U. Morgner, F.X. Kartner, C. Pitris, S.A. Boppart, X.D. Li, E.P. Ippen, J.G. Fujimoto, *In vivo* ultrahigh resolution optical coherence tomography. *Opt. Lett.* **24**, 1221–1223 (1999)
4. A.M. Kovalevich, T. Ko, I. Hartl, J.G. Fujimoto, M. Pollnau, R.P. Salathe, Ultrahigh resolution optical coherence tomography using a superluminescent light source. *Opt. Express* **10**, 349–353 (2002)
5. I. Hartl, X.D. Li, C. Chudoba, R.K. Ghanta, T.H. Ko, J.G. Fujimoto, J.K. Ranka, R.S. Windeler, Ultrahigh-resolution optical coherence tomography using continuum generation in an air-silica microstructure optical fiber. *Opt. Lett.* **26**, 608–610 (2001)
6. B. Povazay, K. Bizheva, A. Unterhuber, B. Hermann, H. Sattmann, A.F. Fercher, W. Drexler, A. Apolonski, W.J. Wadsworth, J.C. Knight, P.S.J. Russel, M. Vetterlein, E. Scherzer, Submicrometer axial resolution optical coherence tomography. *Opt. Lett.* **27**, 1800–1802 (2002)
7. J.M. Schmitt, S.L. Lee, K.M. Yung, An optical coherence microscope with enhanced resolving power in thick tissue. *Opt. Commun.* **142**, 203–207 (1997)
8. A. Baumgartner, C.K. Hitzenberger, H. Sattmann, W. Dresler, A.F. Fercher, Signal and resolution enhancements in dual beam optical coherence tomography of the human eye. *J. Biomed. Opt.* **3**, 45–54 (1998)
9. F. Lexer, C.K. Hitzenberger, W. Drexler, S. Molebny, H. Sattmann, M. Sticker, A.F. Fercher, Dynamic coherent focus OCT with depth-independent transversal resolution. *J. Mod. Opt.* **46**, 541–553 (1999)
10. A. Knüttel, M. Boehlau-Godau, Spatially confined and temporally resolved refractive index and scattering evaluation in human skin performed with optical coherence tomography. *J. Biomed. Opt.* **5**, 83–92 (2000)
11. V.M. Gelikonov, G.V. Gelikonov, N.D. Gladkova, V.I. Leonov, F.I. Feldchtein, A.M. Sergeev, Y.I. Khanin, Optical fiber interferometer and piezoelectric modulator. US 5835642, 1998

12. V.K. Batovrin, I.A. Garmash, V.M. Gelikonov, G.V. Gelikonov, A.V. Lyubarskii, A.G. Plyavenek, S.A. Safin, A.T. Semenov, V.R. Shidlovskii, M.V. Shramenko, S.D. Yakubovich, Superluminescent diodes based on single-quantum-well (GaAl) As heterostructures. *Quant. Electron.* **26**, 109–114 (1996)
13. V.K. Batovrin, I.A. Garmash, V.M. Gelikonov, G.V. Gelikonov, A.V. Lyubarskii, A.G. Plyavenek, S.A. Safin, A.T. Semenov, V.R. Shidlovskii, M.V. Shramenko, S.D. Yakubovich, Superluminescent diodes based on single-quantum-well (GaAl) As heterostructures. *Kvantovaya Elektronika Moskva* **23**, 113–118 (1996)
14. L.S. Dolin, A theory of optical coherence tomography. *Quant. Electron.* **41**, 850–873 (1998)
15. L.S. Dolin, On the passage of a pulsed light signal through an absorbing medium with strong anisotropic scattering. *Izvestiya Vysshikh Uchebnykh Zavedenii, Radiofizika* **26**, 300–309 (1983)
16. D. Huang, E.A. Swanson, C.P. Lin, J.S. Schuman, W.G. Stinson, W. Chang, M.R. Hee, T. Flotte, K. Gregory, C.A. Puliafito, J.G. Fujimoto, Optical coherence tomography. *Science* **254**, 1178–1181 (1991)
17. A.F. Fercher, C.K. Hitzenberger, G. Kamp, S.Y. Elzaiat, Measurement of intraocular distances by backscattering spectral interferometry. *Opt. Commun.* **117**, 43–48 (1995)
18. T. Wilson, *Confocal Microscopy* (Academic, San Diego/London, 1990), p. 426
19. V.M. Gelikonov, G.V. Gelikonov, R.V. Kuranov, N.K. Nikulin, G.A. Petrova, V.V. Pochinko, K.I. Pravdenko, A.M. Sergeev, F.I. Feldchtein, Y.I. Khanin, D.V. Shabanov, Coherent optical tomography of microscopic inhomogeneities in biological tissues. *J. Exp. Theor. Phys. Lett.* **61**, 149–153 (1995)
20. B.E. Bouma, G.J. Tearney (eds.), in *Handbook of Optical Coherence Tomography*, 1st edn. (Marcel Dekker, New York, 2002), p. 741
21. E. Gotzinger, M. Pircher, R.A. Leitgeb, C.K. Hitzenberger, High speed full range complex spectral domain optical coherence tomography. *Opt. Express* **13**, 583–594 (2005)
22. J. Ai, L.V. Wang, Synchronous self-elimination of autocorrelation interference in Fourier-domain optical coherence tomography. *Opt. Lett.* **30**, 2939–2941 (2005)
23. V.V. Tuchin, Optical clearing of tissues and blood using the immersion method. *J. Phys. D (Appl. Phys.)* **38**, 2497–2518 (2005)
24. S.G. Proskurin, I.V. Meglinski, Optical coherence tomography imaging depth enhancement by superficial skin optical clearing. *Laser Phys. Lett.* **4**, 824–826 (2007)
25. I.V. Larina, E.F. Carbajal, V.V. Tuchin, M.E. Dickinson, K.V. Larin, Enhanced OCT imaging of embryonic tissue with optical clearing. *Laser Phys. Lett.* **5**, 476–479 (2008)
26. C.J. Koester, *Handbook of Biological Confocal Microscopy* (Plenum, New York, 1990)
27. T. Zhang, I. Yamaguchi, Three-dimensional microscopy with phase-shifting digital holography. *Opt. Lett.* **23**, 1221–1223 (1998)
28. M.K. Kim, Wavelength-scanning digital interference holography for optical section imaging. *Opt. Lett.* **24**, 1693–1695 (1999)
29. L. Yu, M.K. Kim, Wavelength-scanning digital interference holography for tomographic three-dimensional imaging by use of the angular spectrum method. *Opt. Lett.* **30**, 2092–2094 (2005)
30. J. Lademann, J. Shevtsova, A. Patzelt, H. Richter, N.D. Gladkova, V.M. Gelikonov, S.A. Gonchukov, Optical method for the screening of doping substances. *Laser Phys. Lett.* **5**, 908–911 (2008)
31. D.V. Shabanov, G.V. Gelikonov, V.M. Gelikonov, Broadband digital holographic technique of optical coherence tomography for 3-dimensional biotissue visualization. *Laser Phys. Lett.* **6**, 753–758 (2009)